Focused ion beam milling of diamond: Effects of H_2O on yield, surface morphology and microstructure

D. P. Adams,[a] M. J. Vasile, T. M. Mayer, and V. C. Hodges
Thin Film, Vacuum and Packaging Department, Sandia National Laboratories, Albuquerque, New Mexico 87185

The effects of H_2O vapor introduced during focused ion beam (FIB) milling of diamond(100) are examined. In particular, we determine the yield, surface morphology, and microstructural damage that results from FIB sputtering and H_2O-assisted FIB milling processes. Experiments involving 20 keV Ga^+ bombardment to doses $\sim 10^{18}$ ions/cm^2 are conducted at a number of fixed ion incidence angles, θ. For each θ selected, H_2O-assisted ion milling shows an increased material removal rate compared with FIB sputtering (no gas assist). The amount by which the yield is enhanced depends on the angle of incidence with the largest difference occurring at $\theta = 75°$. Experiments that vary pixel dwell time from 3 μs to 20 ms while maintaining a fixed H_2O gas pressure demonstrate the additional effect of beam scan rate on yield for gas-assisted processes. Different surface morphologies develop during ion bombardment depending on the angle of ion incidence and the presence/absence of H_2O. In general, a single mode of ripples having a wave vector aligned with the projection of the ion beam vector forms for θ as high as 70°. H_2O affects this morphology by lowering the ripple onset angle and decreasing the ripple wavelength. At high angles of incidence ($\theta > 70°$) a step/terrace morphology is observed. H_2O-assisted milling at $\theta > 70°$ results in a smoother stepped surface compared with FIB sputtering. Transmission electron microscopy shows that the amorphized thickness is reduced by 20% when using H_2O-assisted FIB milling. © *2003 American Vacuum Society.* [DOI: 10.1116/1.1619421]

I. INTRODUCTION

Focused ion beam (FIB) sputtering[1] is a technique that is currently used to modify microdevices and fabricate microtools. FIB methods are attractive for machining at the microscale, since these can shape almost any solid including hard materials. In addition, focused ion beams are beneficial, because negligible force and heat are imposed on a target during fabrication. Nanoamperes are, typically, used during focused ion milling, and the range of 10–30 keV ions in solids is small, approximately a few hundred angstroms. Micron-scale features are precisely shaped with nanometer precision, because current FIB systems maintain a small beam size (5–1000 nm), excellent beam positioning accuracy, large depth of focus, and stable operating conditions.[1] When combined with a multiaxis stage having rotation,[2] this micromachining technique can be used to sculpt geometrically complex objects. An example 20-μm-wide, diamond cutting tool shaped by focused ion beam sputtering is shown in Fig. 1.

Processes such as FIB sputtering that fabricate diamond and related materials are of interest for improving micronscale devices, sensors, and instruments.[3–10] Various applications benefit from the use of diamond, because it has a high thermal conductivity, negative electron affinity, and a relatively large band gap. For microtools and indenters, a high yield strength and chemical inertness at low temperature are germane. Diamond has the highest hardness (~ 100 GPa) of any material found in nature.[11,12]

Despite interest in diamond, processes that shape this material by sputtering suffer from a low removal rate. High energy (20–50 keV), focused ion beam sputtering at normal incidence is characterized by a yield$= 0.09$ μm^3/nC, corresponding to ~ 2 atoms/ion.[13–15] Using the maximum current afforded by commercial FIB systems (20 nA), diamond can be sculpted at a rate of ~ 1.8 μm^3/s. A low sputter rate is attributed to a high C–C surface binding energy equal to 7.5 eV.[16]

Several advances have been made to improve the "ion beam machinability" of diamond. A common strategy to enhance the yield of this or other low sputter rate materials involves exposure of the bombarded area to a reactive gas (a process referred to broadly as chemical-assisted etching). As described by Harriott,[17] for most applications an ideal chemical-assist gas increases the rate of sputter removal, minimizes the effects of redeposition, and reduces implantation of the primary ion species in a sample. Previous research shows that a reactive gas can increase the material removal rate by lowering the binding energy of surface species thereby generating volatile etch products, or by changing the dynamics of the ion-generated collision cascade.[18] Chemical-assisted etching processes specific to diamond have been reported by several groups.[13,14,19–22] Early work by Efremow *et al.*[19] with Xe^+ ion beams showed a $10\times$ increase in material removal rate when using a reactive flux of NO_2. Russell *et al.*[14,20] more recently showed that a less hazardous gas, H_2O, can be used to significantly enhance the rate of diamond milling. Introduction of H_2O during 25 keV Ga^+ bombardment of C at $\theta = 0°$ (normal incidence) led to a $5-11$ $\times$ enhancement in material removal rate compared with simi-
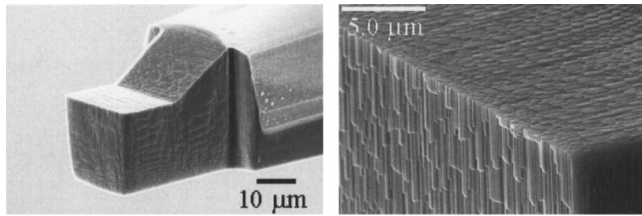
[a]Electronic mail: dpadams@sandia.gov

FIG. 1. Focused ion beam shaped, diamond microtool for ultraprecision lathe turning operations. The tool has cutting edge radii of curvature (Ref. 3) equal to 40 nm. Image on right shows intersection of three FIB sputtered surfaces at high magnification. All surfaces are created by sputtering near-grazing incidence.

lar ion beam processes having no chemical assist.[20,21]

A more complete understanding of H_2O-assisted ion milling is required for tailoring the shape of future diamond instruments. Microtools having curved surfaces (e.g., hemisphere) and small surface roughness are of interest for indentation and ultraprecision machining. In order to control curved shapes accurately by FIB, we require knowledge of the material-specific, sputter yield angular dependence, $Y(\theta)$.[23] A FIB technique put forth by Vasile *et al.*[24] converts an initially planar surface into predetermined curved shapes in a single mill step. However, this procedure requires knowledge of $Y(\theta)$ when solving numerically for required pixel dwell times. In general, we must determine $Y(\theta)$ for the exact conditions used during FIB processing, including the presence of an assist gas (if used). The surface morphology that develops during FIB milling is also important for diamond applications. For example, the six-sided diamond microtool shown in Fig. 1 exhibits a distinct step/terrace morphology on surfaces sputtered at near-grazing incidence angles ($\theta \sim 88°$). Fabrication of a smooth, highly curved surface can be more difficult, as shown in Fig. 2 for a microindenter tip. This tool is nominally shaped by FIB sputtering into a hemisphere starting from a flat face on a near-cylindrical blank. By maintaining the scanned beam parallel to the tool axis, a variety of morphological features evolve at different angles of incidence including: smooth surfaces at $\theta < 40°$, ripples at $40° < \theta < 75°$, and a step/terrace topography at $\theta > 70°$.

For this study, we analyze yield, surface morphology, and changes in microstructure for ion bombardment at different
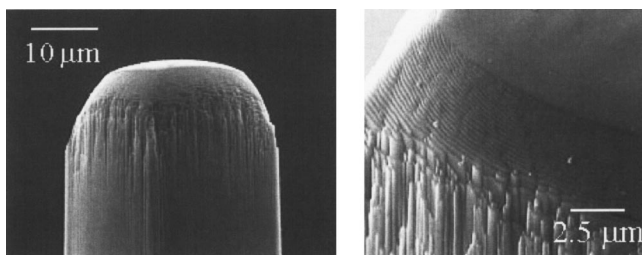

FIG. 2. Prototype FIB-shaped, single crystal diamond, curved tip microindenter. The focused ion beam is scanned across the stationary tool with the ion beam vector parallel to the tool axis. The pixel dwell time is varied to tailor net shape. On right is a high magnification view of the same tool showing three unique surface morphologies. No assist gas is used.

angles of incidence, θ, with and without H_2O assist. High doses, $\sim 10^{18}$ ions/cm^2, are chosen, because previous work[15] shows that diamond attains a near-constant, normal incidence sputter yield at these values. High dose experiments, therefore, allow for a meaningful comparison of the two FIB techniques and identification of H_2O-induced effects.

II. EXPERIMENTAL APPARATUS

A custom-built focused ion beam system is used for ion milling experiments.[25] The target chamber has a base pressure of 1×10^{-7} Torr and contains a precision $x-y$ stage, a sample cassette, a custom-built gas doser, a secondary electron detector, and a residual gas analyzer. The ion column is located in a separate chamber that is differentially pumped by a Varian diode ion pump to a base pressure of $< 1 \times 10^{-8}$ Torr. A beam of gallium ions is generated from a liquid metal ion source (FEI, Inc.) and directed onto the target using a single lens column. During operation the pressure in the ion beam column may rise to 2×10^{-8} Torr, or as high as 5×10^{-8} Torr when using a H_2O doser. The ion beam energy is 20 keV for all experiments, and a fixed current of 2.8 nA (measured in a Faraday cup) is selected. The beam shape is determined by scanning electron microscopy (SEM) to be roughly Gaussian with a full width at half maximum (FWHM) of 0.6 μm. A single-axis rotary stage attachment allows precise control of sample tilt and, therefore, the ion beam incidence angle.[26] An in-vacuum stepper motor and reduction gear assembly can orient a sample through 360° if necessary. Rotation is controlled by a Princeton Research Instruments stepper motor unit. In order to ensure that a particular angle of incidence is selected prior to each mill step, a dial indicator mounted directly onto the rotary stage shaft is viewed using the secondary electron detector. We expect that this arrangement along with procedures for leveling diamond specimens using an interferometric microscope (ADE phase shift MicroXAM) reproducibly establish the angle of incidence, θ, with an uncertainty of $\pm 0.25°$. The angle of ion beam incidence, θ, is defined with respect to the substrate surface normal.

Gas-assisted ion milling involves positioning a 250 μm inner diameter nozzle near the sample surface. An optical microscope is mounted on the outside of the vacuum chamber to check gas jet–sample alignment and to fix working distance (WD) at 250 μm for all gas-assisted ion milling experiments (with the exception of the data shown in Fig. 3). A 250 μm working distance is chosen, because the effects of H_2O for enhancing yield are optimized when positioning the gas jet aperture to a distance approximately equal to the nozzle inner diameter. As demonstrated in Fig. 3 for experiments at $\theta = 0°$ and a pixel dwell time of 65 μs, the yield is constant for working distances between 100 and 250 μm, while spacings greater than 250 μm lead to only a slight enhancement compared with FIB sputtering with no H_2O present. Gas pressure is manually controlled by an ultra-high-vacuum leak valve mounted between a bakeable, stainless steel manifold and the gas jet inlet. A MKS Instruments capacitance manometer gauge (type 628B) indicates 7.1 Torr
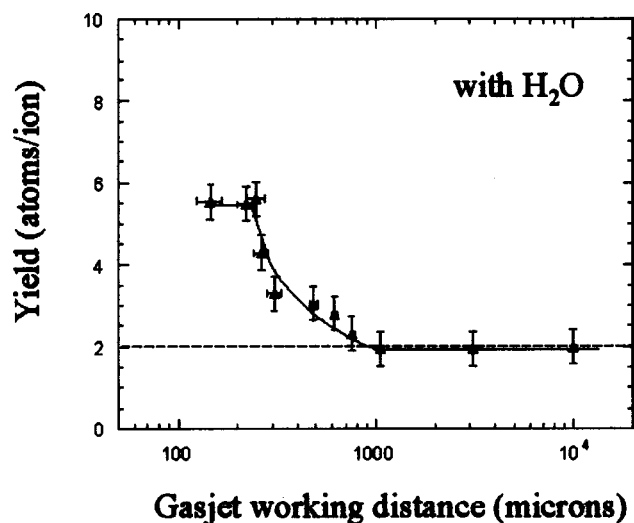
FIG. 3. Plot of yield (C atoms/ion) as a function of gasjet working distance for H_2O assisted ion milling. Dotted line shows the FIB sputter yield (with no gas assist).
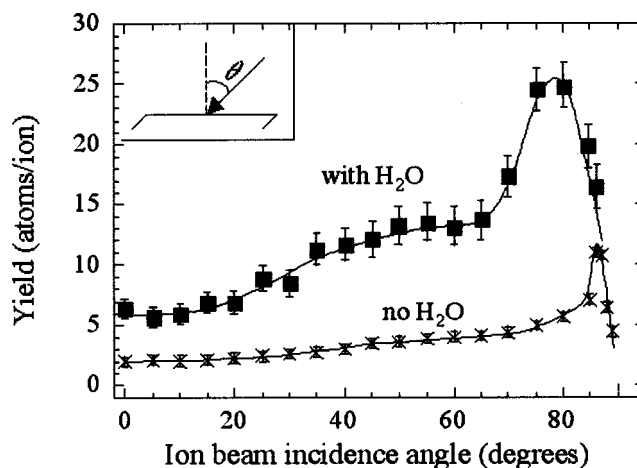

FIG. 4. Plot of yield (C atoms/ion) vs ion beam incidence angle, θ. Two data sets are shown including results from gallium ion beam bombardment ($\times$) and H_2O-assisted processes ($\blacksquare$). The lines shown are guides to the eye. θ is defined with respect to the substrate normal as shown in the inset.

between the leak valve and gas jet during H_2O-assisted experiments. Based on similarities in gas jet–sample geometry with Stark *et al.*,[21] we estimate that the H_2O pressure at the sample surface is 0.1 Torr when using a WD$=250$ μm.

III. RESULTS AND DISCUSSION

A. Yield of diamond: FIB sputtering and H_2O-assisted FIB milling

Experiments determine the angular dependence of yield, $Y(\theta)$, defined as the number of C atoms removed per incident Ga^+ ion. A clean, smooth[27] specimen of single crystal (100) diamond is first mounted and leveled to the plane of the cassette. Once inserted into the vacuum chamber, a sample is tilted to a particular angle, viewed, and bombarded within targeted areas. Our FIB milling procedure involves outlining a square box feature and exposing the area to a focused gallium beam. For experiments at $\theta \leq 80°$, 12 $\times 12$ μm boxes are outlined as viewed in projection by the operator. This 62×62 pixel box defines the area of the diamond surface over which the beam is rastered equal to 12 $\times 12/\cos\theta$ (μm^2). Experiments at angles greater than 80° require 12×6 μm boxes [area$=12 \times 6/\cos\theta$ (μm^2)], because the feature becomes extremely long in one direction. Outlining a box with a reduced y dimension shortens the feature allowing for accurate measurements of sputtered volume after removal from the vacuum system. In addition, H_2O-assist experiments at high θ require a reduced feature length in order to maintain a constant gas pressure across the exposed area. Experiments are designed to keep the ion-milled feature less than 200 μm long when using the 250 μm inner diameter gas jet. Yields are determined at different ion beam incidence angles, typically, in 5° increments. For FIB sputtering experiments, we are also able to measure yield at extremely high angles of $\theta=86°$, 87°, 88°, and 89°. In all cases, the focused ion beam is scanned across the area of

interest in a serpentine pattern. Despite rastering, a uniform ion dose is given to each outlined area. The near Gaussian shaped, 0.6 μm FWHM ion beam is relatively large compared with the pixel spacing of 0.19 μm, thus, providing substantial beam overlap.

Figure 4 shows a plot of the measured yield versus ion beam incidence angle for both FIB sputtering and H_2O-assisted FIB milling processes. For these experiments, we use a pixel dwell time of 130 μs and a refresh time[28] of 351.98 ms. Yield is determined after removing the sample from the vacuum system. The sputtered volume is first measured using a calibrated ADE phase shift MicroXAM interferometric microscope having 1 Å vertical resolution. Interferometry accurately determines milled feature volume; feature depths measured by this technique are nearly identical to those measured by a calibrated atomic force microscope. The yield is equal to $1.602 \times 10^{-19} \times \rho \times V_c/(i_{Ga} \times t)$, where ρ is the density of diamond[29] (1.76×10^{11} atoms/μm^3), V_c is the sputtered cavity volume, i_{Ga} is the beam current measured in a Faraday cup, and t is the exposure time. We expect the yields determined, assuming a density of single crystal diamond, are not greatly affected by a known ion-induced change in crystal structure of the near-surface region. Although transmission electron microscopy shows that the carbon substrate is amorphized to a depth of 10–50 nm (demonstrated later in this report), this thickness is relatively small compared with the feature depth.

FIB sputter yield depends on ion beam incidence angle with the lowest material removal rates occurring at 0° and near 90°. For FIB sputtering, we find $Y(0°)$ equals 2.0, consistent with previous works.[13–15,21] There is a slight increase in sputter yield between 0° and 80° followed by a sharp rise between 80° and 85°. A maximum yield, Y_{max}, is found at 86°. The angle at which $Y_{max}(\theta)$ occurs is in good agreement with TRIM calculations.[30] These simulations confirm that the FIB sputter yield peaks at angles greater than 80° due to the deeply penetrating nature of the high-energy ion beam. Ex-

periments demonstrate a decreased FIB sputter yield for angles greater than 86°. This presumably occurs because of ion reflection. A Ga$^+$ ion will reflect off a smooth surface with higher probability as the angle of incidence approaches 90°. We do not expect redeposition of ejecta complicates our measurements of volume and calculations of FIB sputter yield. The largest FIB sputtered feature depth is 3.65 μm. Therefore, the depth/width aspect ratio of sputtered features is 0.30 or less.

The yield characteristic of H$_2$O-assisted FIB milling is also dependent on ion beam incidence angle but shows a broader peak at high angles compared with FIB sputtering. The milling yield at 0° is 6.4 atoms/ion, and an increase is found with angle up to $\theta = 75°$. For H$_2$O-assisted milling, the peak yield (25 atoms/ion) occurs at an angle $\sim 75° - 80°$. Note, the angle for which $Y(\theta) = Y_{max}$ is less than that for FIB sputtering with no gas assist.

For all angles of incidence probed in this study, H$_2$O leads to an increased yield compared with FIB sputtering and no gas assist. When using a pixel dwell time of 130 μs, the yield is enhanced 1.5–4.8× for angles in the range 0°–86°. The amount by which yield increases depends on the specific angle chosen. The largest difference in yield (4.8×) is found at $\theta = 75°$. Interestingly, at high angles of incidence, above 85°, Fig. 4 shows only a slight difference in the yield for H$_2$O-assisted milling compared with FIB sputtering. For example, at $\theta = 86°$ the yield is only 1.5× that for FIB sputtering. We speculate that the effects of H$_2$O on yield are reduced at extremely high angles, because the adsorbed species are preferentially removed by the ion beam. Direct knock-on collisions with adsorbed species would reduce the surface concentration of reactive gas during a given scan making the interaction and yield similar to that for FIB sputtering. A reduced role of H$_2$O at very high angles may, in part, explain the smaller angle for which the maximum material removal rate is observed. We recognize that surface morphology may also affect the yield at high θ. As first observed by Russell *et al.*,[14] the introduction of H$_2$O leads to a dramatically smooth surface compared with that produced by FIB sputtering at high incidence angles. The difference in step density may thereby lead to a vastly different ion reflection coefficient, and this could contribute to a decreased yield at high angles.

Measurements of $Y(0°)$ for H$_2$O-assisted milling are consistent with Russell *et al.*,[14] even though our value, 6.4 atoms/ion, is considerably less than that reported previously. This discrepancy is explained in the next section as being due to different ion beam pixel dwell times. The 130 μs dwell time used for experiments highlighted in Fig. 4 was chosen more for convenience than for optimizing yield. Strategies for gas-assisted milling at maximum rates are developed by fixing the gas pressure at a reasonably high value and varying the pixel dwell time over a large range.[31,32]

B. Effect of pixel dwell time on yield for H$_2$O-assisted FIB milling

Enhancement of etching by reactive gases has been modeled previously as a function of ion/neutral flux ratio and
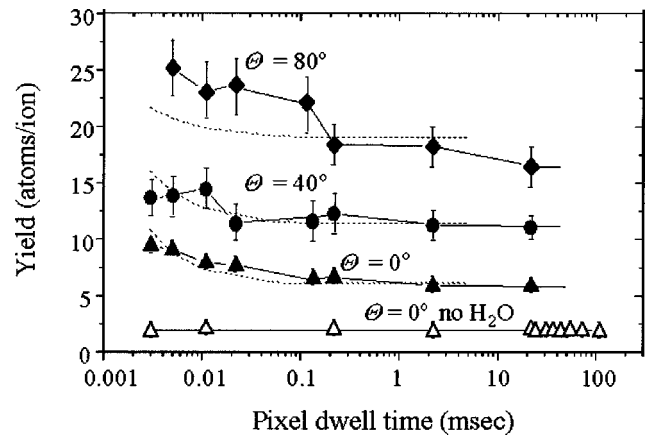

FIG. 5. Plot of yield (C atoms/ion) vs pixel dwell time for H$_2$O-assisted FIB milling of diamond (filled symbols) and FIB sputtering ($\triangle$). Milling experiments at three different angles of incidence show the influence of pixel dwell time when using a fixed H$_2$O pressure. Dotted lines shown are simulated yields.

reactive gas coverage.[33,34] For the case of a focused beam rastered over a surface, continuous gas adsorption will occur in a given pixel, while material removal occurs only when the beam is on that pixel. Reactive gas is also removed during sputtering, such that the average surface coverage by reactive species depends on the pixel dwell time; we may expect that the observed etch yield will depend on the pixel dwell time. This has indeed been observed by Stark *et al.*[21] in focused ion beam etching of PMMA using H$_2$O as a reactive gas.

In Fig. 5 we show that yield increases with decreasing pixel dwell time for H$_2$O enhanced etching, while there is no change in yield in the absence of H$_2$O. The origin of this effect is shown quite simply by considering the adsorption and ion-induced desorption kinetics of reactive gas. During the beam-off period gas adsorbs to the surface and the fractional coverage, C, can be described by a simple Langmuir adsorption process:

$$dC/dt = sf_n(1-C), \tag{1a}$$

where s is a sticking coefficient and f_n is the flux of neutral species to the surface. Adsorption continues up to a monolayer and saturates when adsorption sites are exhausted. During the beam-on period reactive species adsorb, as above, and are removed by sputtering. Some fraction of the removed species contains a substrate atom, and thus result in etching. The fractional coverage of gas then is described as

$$dC/dt = sf_n(1-C) - bf_iC, \tag{1b}$$

where b is the ion yield of reactive gas species (including carbon containing products), and f_i is the ion flux. The total etch yield, Y_{total}, is then the summation of the chemically enhanced etching yield and the physical sputtering yield:

$$Y_{total} = jbC + Y_s(1-C), \tag{1c}$$

where j is the fraction of reactive product species that contains a carbon atom, and Y_s is the sputter yield in the absence of chemical enhancement.[34] For simplicity, we write the re-

active etch yield as proportional to the surface coverage, assume all reactive products contain carbon ($j=1$), and assume simple Langmuir adsorption kinetics. In reality, the situation may be more complicated due to surface alteration by ion mixing, and other ion bombardment induced effects that change the surface composition over the range of ion penetration. The chemically enhanced yield, b, strictly refers to removal of adsorbed gas, not to removal of substrate atoms, so the actual yield of substrate atoms will be less than b, and depend on the stoichiometry of the etch products. The sticking coefficient of reactive gas may also be different during the beam-on and beam-off periods due to the effects of ion bombardment in producing defects and dangling bond sites, which are known to increase surface reactivity.[34] The yield parameters are also dependent on ion beam incidence angle. Despite these complications, this simple model has been shown effective at describing ion-enhanced etching of Si and SiO_2 in steady state plasma conditions.[33–35] We will show here that it also accounts for the yield dependence on pixel dwell time shown in Fig. 5 and in Stark's work.[21]

The beam is rastered over a 62×62 pixel array within the 12×12 μm box,[36] and the 0.6 μm FWHM beam overlaps about five pixels at a time. Considering this pixel overlap we estimate the relative on/off periods of the beam as 1/1536. Using Eq. (1a), we calculate the surface coverage achieved during the beam-off period, then use Eq. (1b) to calculate the coverage during the beam-on period. During the beam-on period the coverage is reduced by sputtering, and the etch yield in Eq. (1c) is obtained from the average coverage during the beam-on period. Using the ion and neutral fluxes of the experiment, assuming unit sticking probability, and using the measured sputter yield in absence of H_2O enhancement, Y_s, we calculate the surface coverage and total etch yield, using the H_2O-enhanced yield, b, as the single adjustable parameter. Shown, also, in Fig. 5 are the calculated yields as a function of pixel dwell time, using H_2O-enhanced yields of 40, 40, and 25 for incidence angles of 0°, 40°, and 80°, respectively. The major effect noted in these simulations is that depletion of the reactive species coverage by sputtering during the beam-on period results in low average surface coverage for long pixel dwell times. Sufficient gas flux is available to saturate the surface during the beam-off period, but in these conditions of relatively low neutral/ion flux ratio, the surface is depleted of reactive species by sputtering for all but the highest angle of incidence (where the ion current density is low), and the average coverage is low. Short dwell times result in less depletion, and thus larger average coverage and higher etch yield. At long dwell times the yield is characterized by the steady state water coverage, similar to what would be observed in a reactive ion etching process at similar ion/neutral flux ratio.

The magnitude of the chemically enhanced yields used to fit these data seem reasonable. The interpretation being that at saturated water coverage, 40 carbon atoms should be removed per ion at normal incidence. The observed yields are substantially lower, because the average H_2O concentration during the beam-on period is, typically, well below satura-

tion. This is realistic, but we should note a number of limitations of both the model and the experiment. First, we cannot independently measure surface coverage, so we must imply that all H_2O is removed from the surface by reaction with C ($j=1$). We know that this is unlikely, but do not have a method for measuring the coverage or the composition of sputtered species. Second, we assume that H_2O adsorbtion saturates at a monolayer. There is evidence that multilayers of H_2O can adsorb, and the effects of ion mixing can result in substantially larger concentrations of reactive species incorporated into subsurface layers as well.[18,37,38] These ion-mixing effects are known to be greater at near-normal incidence, hence, the larger effect at 0° and 40° as compared to 80°. Third, we assume that the yield of carbon sputtered from areas not covered by water is the same as the yield observed in the total absence of water. The alteration of the surface layer by H_2O incorporation and ion damage may significantly change the surface binding energy of C, and hence the yield, even if no adsorbed water is present. Despite these complications, this simple model describes in a straightforward way the dependence of etch yield on pixel dwell time. The obvious strategy to achieve the highest etch yield is to use as high a neutral/ion flux ratio as possible, and the shortest possible dwell time to maintain high surface concentration of reactive species.

The yields for H_2O-assisted FIB milling at 0° shown in Fig. 5 are less than the value determined by Russell *et al.*[14] because of the different pixel dwell times used in the two sets of experiments. Russell reports a pixel dwell time of 0.5 μs for their experiments and determines a yield of 14.4 atoms/ion. Extrapolation of the $\theta=0°$ data set shown in Fig. 5 to dwell times ~0.5 μs predicts a yield >10 atoms/ion.

As a final note, previous work has shown that an increased material removal rate can be induced at high pixel dwell times when the depth removed per pixel is similar in dimension to the beam width.[39] This effect, which can occur with or without gas assist, is due to formation of a facet with a locally higher angle of incidence and higher yield (as in Fig. 4). However, this does not occur to a large degree in our experiments, since the ion beam FWHM is considerably larger than the depth removed per pixel even for the largest pixel dwell times.

C. Surface morphology and effects of H₂O

Different surface morphologies develop during ion bombardment depending on the angle of incidence and the presence/absence of H_2O. As shown in Figs. 2 and 6, three distinct morphologies are observed: smooth surfaces, ripples, and a step/terrace topography. The dotted lines shown in the two plots of Fig. 6 bound ranges of angles where surfaces show one of the three distinct shapes. Figure 6 also displays the roughness measured by a Digital Instruments Dimension 5000 atomic force microscope using a ~5 nm radius tip. The roughnesses are obtained by scanning 5×5 μm areas in the center of ion milled features.

For θ less than 40°, FIB sputtering and H_2O-assisted milling generate smooth surfaces. The roughness of ion bom-
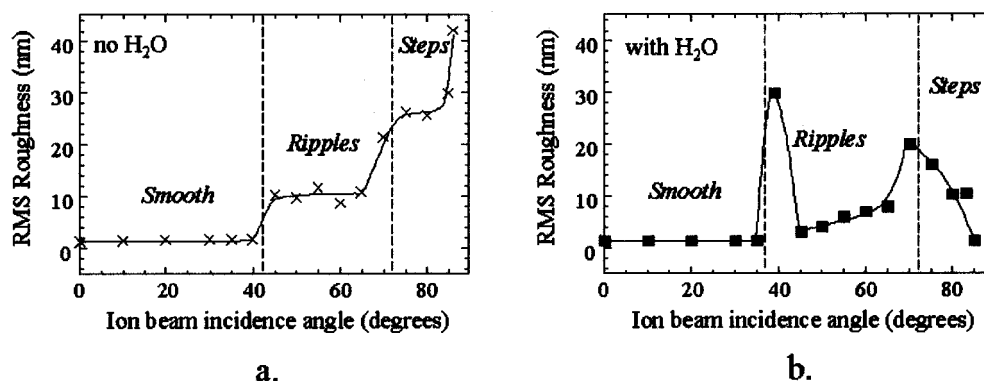
FIG. 6. Plots of root mean squared surface roughness (R_{rms}) vs angle of incidence for (a.) FIB sputtering and (b.) H$_2$O-assisted FIB milling. Measurements of roughness and determination of morphology involved atomic force microscopy.

barded surfaces is small with $R_{rms} \sim 1.5$ nm for both processes. Comparison of the surface roughness in the bottom of ion bombarded features to that of the surrounding areas not exposed to the beam shows that the milled surfaces are smoother. These observations are consistent with a previous investigation of FIB sputtered diamond.[40]

At higher angles of incidence, ripples develop during FIB sputtering and H$_2$O-assisted FIB milling. The formation of ripples during oblique ion bombardment has been observed previously for a number of material systems,[41–43] and models have been proposed to explain ripple frequency and amplitude as a result of ion scattering parameters and surface transport processes.[44,45] Ripples grow as a result of a surface instability induced by a subtle dependence of sputter yield on surface curvature.[44] Smoothening mechanisms can include thermal diffusion,[44,46] viscous flow,[47] ion-enhanced diffusion,[48,49] and preferential sputtering without mass transport.[45] Thermal diffusion on diamond at 30 °C is unlikely,[50] but the fact that we observe surface smoothing at normal incidence (where ripples do not form) suggests that some ion enhanced transport process is involved. In these experiments an amorphous layer near the surface is formed by ion bombardment (see the following section), so viscous flow as well as ion enhanced surface diffusion is possible. However, we cannot distinguish between these two ion-induced processes. A more comprehensive examination of ripple formation and evolution with dose is presented in another article.[51]

Ripples developed during FIB sputtering[40] and H$_2$O-assisted FIB milling have a wave vector aligned with the projection of the ion beam vector. Figure 7 shows atomic force microscope images of rippled surfaces formed at $\theta = 55°$ demonstrating this single habit that continues to high θ. A second mode of ripples having a perpendicular orientation is found in other experiments and is predicted by Bradley and Harper,[44] but we find no evidence for a transition to ripples having this orientation. We show in a separate study[51] that for 20 keV Ga$^+$ the transition to perpendicularly oriented ripples is predicted to occur near 73°. Essentially, the deposited energy distribution resulting from Ga ion bombardment extends the transition in ripple habit to relatively

high angles, compared with that for low energy ion bombardment.[52] Above 70° we observe the transition from parallel ripples to a distinct step/terrace structure. This sawtooth-like morphology is evidence that shadowing becomes important at $\theta > 70°$. Shadowing between isolated surface morphological features occurs, because a critical feature height/length ratio is exceeded, thereby preventing ion beam exposure to parts of the surface.[53] The result is planarization of the peaks on the surface and formation of distinct terraces and step risers. It is apparent that shadowing and the formation of a step/terrace morphology thereby precludes the onset of ripples having a perpendicular orientation in diamond. We expect this to be a general phenomenon in other materials FIB sputtered at high energy.

Although FIB sputtering and H$_2$O-assisted FIB milling both generate ripples of a single orientation, there are noticeable differences in morphology formed by the two processes. First, the lowest angle at which ripples develop is different for FIB sputtering compared with reactive milling. For FIB sputtering (no gas assist) we find ripples beginning at $\theta = 45°$. This is consistent with previous work by Datta *et al.*[54] at 10 and 50 keV. With the addition of H$_2$O, ripples clearly form at a smaller angle $\theta = 40°$. Although the ripple onset angle has previously been observed to change with ion beam energy,[54] we believe that this is the first report showing a

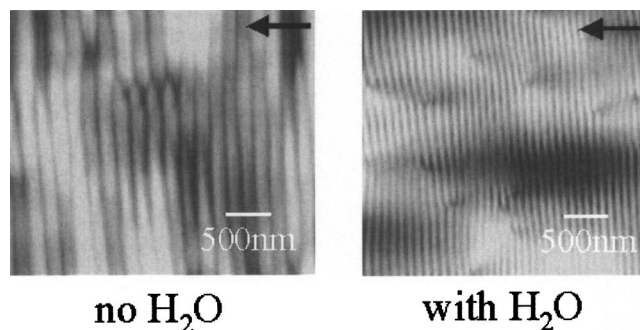**no H$_2$O**   **with H$_2$O**

FIG. 7. AFM images of diamond surface FIB sputtered (left) and FIB milled in the presence of H$_2$O (right). Experiments involved a single ion beam incidence angle, $\theta = 55°$, and a fixed dose of 1×10^{19} ions/cm^2. Arrows indicate the projection of the ion beam vector.
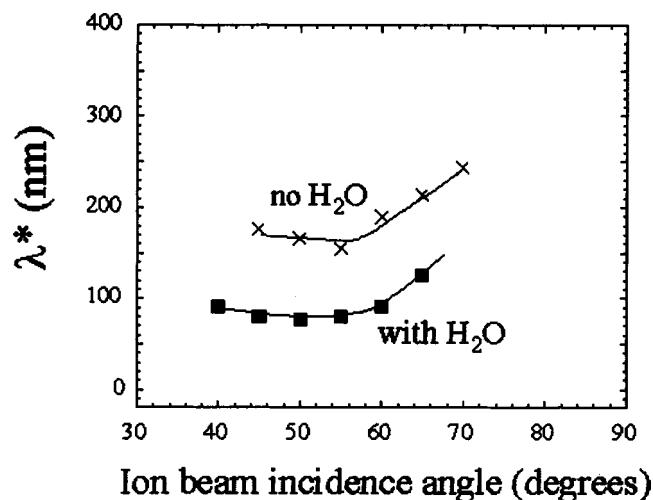
FIG. 8. Plot of saturation ripple wavelength (λ*) versus ion beam incidence angle. This contrasts λ* for FIB sputtering ($\times$) and H_2O-assisted FIB milling ($\blacksquare$).

FIG. 9. Scanning electron micrograph of surface FIB milled in the presence of H_2O at $\theta = 40°$. High frequency ripples ($\lambda \sim 90$ nm) are seen in addition to large amplitude, long wavelength ($\lambda \sim 1000$ nm) ridges. The long wavelength features are only seen when using H_2O assist and are most prominent at $\theta = 40°$.

change in angle due to the presence of a reactive gas. Other differences in ripple morphology are apparent by atomic force microscopy (AFM). Comparisons of surfaces show that H_2O-assisted etching on average leads to a reduced ripple wavelength and amplitude. The two images shown in Fig. 7 compare FIB sputtered and reactively milled surfaces for a single angle of incidence, 55°. We find in a separate study of evolving ripple shape with increasing dose[51] that a near-constant wavelength characterizes the surface morphology at high ion doses. This evolution to a steady-state morphology is observed in other materials and appears to be a somewhat general behavior.[40,43] Figure 8 shows the saturation wavelength, λ*, as a function of incidence angle. For all angles the saturation wavelengths for FIB sputtering are larger than that developed during H_2O-assisted FIB milling.

We argue that the differences in ripple wavelength produced by the two processes are due to reactive gas adsorption and its effect on increasing yield.[51] The roughening prefactor described by Bradley and Harper[44] is proportional to yield, and the λ* derived (for the case of thermal diffusion) is inversely related to the square root of $Y(\theta)$. Assuming that a similar relationship exists for the case of ripple development in carbon, the higher gas-assisted milling yields shown in Fig. 4 for θ between 45° and 65° should lead to a decrease in λ* by as much as a factor of 2. This is precisely the result shown in Fig. 8 when comparing results from FIB sputtering and H_2O-assisted milling. For each θ studied, the saturation wavelength is decreased by approximately a factor of 2 when H_2O is present.

A curious surface morphology develops at $\theta = 40°$ when using H_2O (see Fig. 9). At this angle H_2O-assisted etching leads to a dramatically rougher surface than for FIB sputtering with no gas assist ($R_{rms} = 30$ nm compared with $R_{rms} = 1$ nm). Ripples develop during H_2O-assisted ion milling at 40° with wavelengths similar to those observed at higher angles. Additionally, we observe very large amplitude, poorly aligned ridges, with much longer wavelengths than
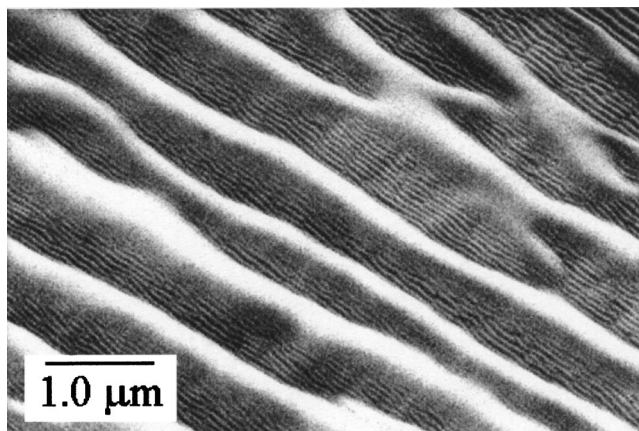
the well-oriented ripple structures shown. The large amplitude ridges dominate the surface roughness spectrum at 40°, leading to the anomalous rms roughness value shown in Fig. 6(b). Ridges are still evident in the morphology observed at higher angles, but not nearly to the extent as at 40°. We do not know the nature of the dynamic processes driving this development. We observe an interesting effect of pixel dwell time on surface morphology evolution at 40°. The very large amplitude, low frequency surface features are apparent at short dwell times but disappear at long dwell times. As noted earlier, for long dwell times the average surface coverage by water is low, and most etching takes place at relatively "dry" sputtering conditions. The development of this gross morphology is evidently an effect of water adsorption during sputtering, and is most prominent at conditions of high surface coverage. The reason why the effect is confined primarily to angles near 40° is also unknown.

At high angles of incidence ($\theta > 70°$) a step/terrace morphology is observed. This is highlighted in Fig. 10 for surfaces FIB sputtered at 75° and 86°. This different morphology more closely resembles a sawtooth wave form rather than a sinusoid ripple formed at lower angles. Transmission electron microscopy (TEM) images in Figs. 11 and 12 further contrast the two types of morphology formed at different angles. A step/terrace morphology is an accurate description of the surface formed at high angles compared with previous discussions of this being a "facetted" shape.[53] While the TEM in Fig. 12 shows well-defined terraces, step risers have curved profiles and a range of angles with respect to the ion beam vector.

A step/terrace morphology is explained by shadowing between neighboring surface morphological features.[53] Shadowing can occur because of texture initially present on the surface or possibly ripples that develop for some short period of time.[53] We have found that a step/terrace morphology can evolve from an initial ripple morphology as the amplitude of the ripples grows at angles around 75°.[55] Essentially, be-
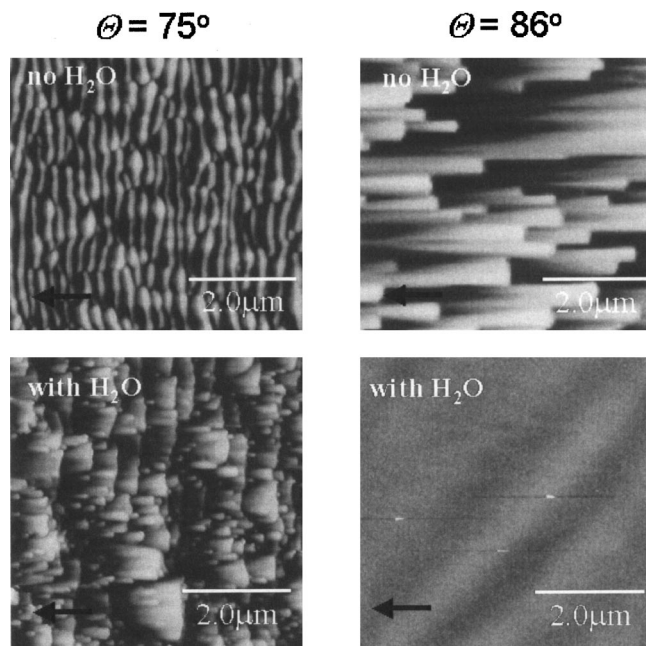
$\Theta = 75°$

$\Theta = 86°$

FIG. 10. AFM images of diamond after FIB sputtering (with no H$_2$O) and milling (with H$_2$O) at two angles of incidence. All images are taken on a 100 nm vertical scale.

FIG. 12. Transmission electron micrographs showing FIB sputtered surface in cross section. Sputtering involved $\theta = 80°$ and a dose of 10^{17} ions/cm^2. Step/terrace morphology is evident along with a damaged layer that varies in thickness from step riser to terrace. The beam direction is indicated by an arrow.

cause the beam is approaching at such a high angle, it will not access all of the surface if features of a certain height/length ratio are present. The ion flux preferentially sputters the peaks of the protrusions and local planarization occurs. The surface then evolves to have a step/terrace morphology.[53] Carter has shown that a critical height to wavelength ratio exists where shadowing sets in at a particular incidence angle.[53] This amplitude to wavelength ratio is given by

$$A/\lambda \leq 1/2\pi \tan(\pi/2 - \theta).$$

At a fixed angle terraces will be longer if the amplitude is increased. After high doses, terraces of greater length win out at the expense of shorter length terraces that exist for only a brief time.

We also observe that the average terrace length changes with θ for both FIB sputtering and H$_2$O-assisted FIB milling.

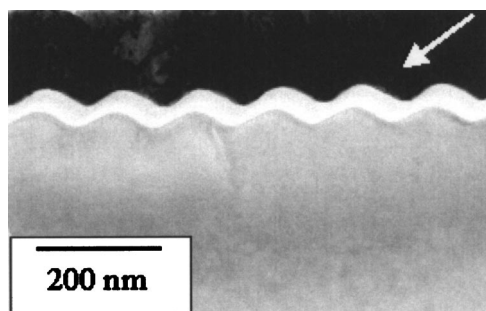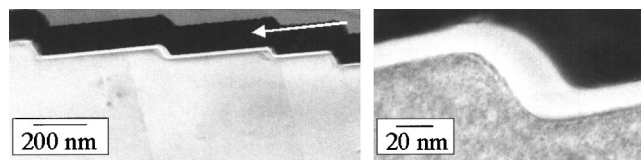FIG. 11. Transmission electron micrograph of rippled surface. This sample was FIB sputtered at $\theta = 55°$, and the amorphized region formed as a result of ion beam damage appears as a "bright" feature. The beam direction is indicated by an arrow.

Terraces are longer as the angle of incidence is increased. This is indicated in Fig. 10; FIB sputtering at 75° results in terraces that are 0.2–0.5 μm long, while for $\theta \sim 86°$ FIB sputtered surfaces have terraces that are 2–20 μm in length. AFM also shows that the terraces are parallel to the ion beam at high ion doses. In this case ions incident on the terraces at very high grazing angles will likely be reflected and impact the next step riser. In the extreme case, all ions eventually impact on step risers. The step riser will move laterally over the surface with a rate determined by the sputter yield at the local angle of incidence on the step riser. In this scenario, the terrace length will be determined by the height of the step riser and the critical angle for sputtering.

As indicated in Figs. 6 and 10, introduction of H$_2$O during ion bombardment dramatically reduces the amplitude of the step risers and the overall surface roughness.[14] For increasing angle greater than 70°, the surface roughness decreases for H$_2$O-assisted milling, while FIB sputtering leads to increasingly rough surfaces up to 86°. At 85° the reactively milled surface has a $R_{rms} = 1.0$ nm, a 30-fold reduction in roughness compared with that for sputtering.

We suggest that the $Y(\theta)$ for a given process is responsible for the differences shown in Fig. 10 at 86°. Specifically, the difference in yield at localized microscale sites on the surface will give rise to a different steady-state (high dose) morphology. Based on the images shown in Fig. 10, a difference in sputter yield must exist for the step riser versus the terrace for the case of FIB sputtering. In this way, a step riser can be slow to propagate across the surface and the surface develops roughness. For the case of H$_2$O-assisted milling we expect more similar sputter yields at different sites on the surface. In order to assess the real difference in sputter yield on a riser versus a terrace, one must determine yield at each particular angle when using a flat target surface. Real time dynamic observations of the surface morphology would aid in the understanding of H$_2$O-assisted smoothing of the ion milled diamond surface. A more complete study should probe lateral step velocities as a function of step height.

D. Microstructure and effects of H$_2$O

Cross section transmission electron microscopy shows that high-energy ion bombardment amorphizes the near-surface region of diamond substrates. A damaged layer is evident in Figs. 11 and 12 for FIB sputtering at 55° and 80°, respectively. TEM also indicates a variation in amorphous
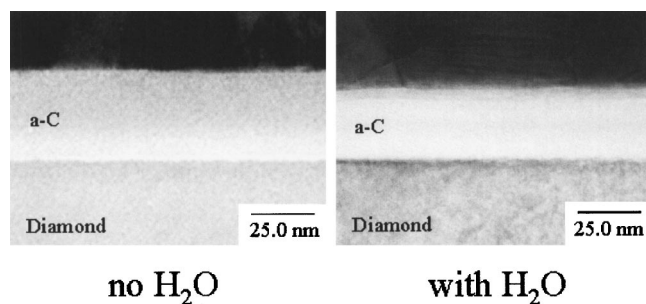
FIG. 13. Transmission electron micrographs showing the damage layers resulting from FIB sputtering (left) and H_2O-assisted FIB milling (right). Sample was bombarded with Ga^+ at $\theta = 0°$ to 10^{18} ions/cm^2. "a-C" indicates the damaged region.

thickness at different sites on rough surfaces. In general, a larger amorphous thickness develops at sites having a small local angle of incidence with respect to the ion beam. A clear example of this is seen in Fig. 12 where the step riser has an amorphous thickness of approximately 30 nm and the terrace (at near grazing incidence) is damaged to a depth of 12 nm. TEM also shows no evidence that surface morphological features are aligned to low Miller index orientations of the crystalline substrate. This includes the terraces formed at $\theta > 70°$, which tend to align close to the direction of the ion beam vector.

The effects of H_2O on microstructure are also revealed by TEM. In general, a 20% reduction in the amorphous thickness is found when using gas-assisted FIB milling. Figure 13 shows an example of this for bombardment at $\theta = 0°$. We choose this angle for analysis, because a smooth surface and uniform amorphous carbon layer thickness are developed. Control experiments show that H_2O does not spontaneously etch a FIB-damaged carbon surface. No change in feature depth was observed after exposing a premilled surface to a flux of H_2O for many minutes (with the ion beam off). Therefore, we can expect that the reduction in layer thickness is an effect of reactive sputtering. The difference in amorphized thickness is consistent with an enhanced material removal rate for H_2O-assisted processes compared with FIB sputtering.

IV. SUMMARY

FIB sputtering and H_2O-assisted FIB milling of initially single crystal diamond surfaces result in very different yields (defined as the number of C atoms removed per incident gallium ion). Consistent with Russell *et al.*[14] we find an increase in material removal rate when using H_2O-assisted processes. This is now demonstrated across a broad range of angles with the enhancement in yield depending on the specific angle chosen. We find large yield enhancements at $\theta \leq 75°$, yet water has a small effect on yield at very high angles of incidence ($\geq 85°$). Possible explanations for this are discussed. The enhancement in yield due to H_2O also depends on ion /neutral flux. A strategy for maximizing the yield involves selecting a small pixel dwell time.

The surface morphology developed during ion bombardment changes with ion beam incidence angle and the addition of H_2O. We find a single mode of ripples to high angles of incidence for both FIB sputtering and H_2O assisted FIB milling. This single ripple habit is due to the deeply penetrating nature of high-energy ions and is predicted to occur in other material systems that exhibit a ripple morphology when using similar beam energies and ion species. H_2O affects this morphology in two ways. First, it lowers the angle of ripple onset. Ripples form at 40° when using H_2O-assisted milling techniques, whereas FIB sputtering generates ripples beginning at 45°. Furthermore, a reduced saturation ripple wavelength results from H_2O exposure. A reduced wavelength is explained by an increased $Y(\theta)$ when using H_2O-assisted milling. Dramatic differences in step/terrace morphology are found for angles $>70°$. Surfaces are smoother when using H_2O for all angles $\theta > 70°$.

Strategies for diamond microfabrication can be developed from the observations made in this work and previous studies. Microfabrication time can clearly be reduced by choosing the angle at which a maximum yield occurs or by adding H_2O vapor. The effects of H_2O on yield are further increased when selecting small pixel dwell times. Nevertheless, H_2O-assisted milling techniques offer only a limited improvement in surface finish. If a smooth surface is desired one can work in the range of angles ($\theta < 40°$ or $\theta \geq 85°$) where no ripples or steps develop. High-angle, H_2O-assisted FIB milling is useful for making smooth surface, planar cuts. On the other hand, fabrication of curved surfaces to intermediate angles requires careful thought. A smooth-surface, hemispherical or parabolic microindenter will be difficult to fabricate from an initially flat-face tool blank if the ion beam vector is kept parallel to the axis of the indenter. For fabricating curved shapes, angles $>40°$ lead to undesired roughness that cannot be overcome solely by the addition of H_2O. Note, fabrication of nanoscale indenters, such as those having diameters less than a single ripple wavelength, may show different morphologies than those presented here.

Alternatively, recipes have now been developed that reproducibly create patterned surfaces of different shape. The formation of a regular array of ripples having a well-defined wavelength and amplitude and a step/terrace morphology having a distribution of terrace lengths could find use as a surface templating technique for subsequent thin film growth.

ACKNOWLEDGMENTS

[1] J. Orloff, Rev. Sci. Instrum. **64**, 1105 (1993).
[2] M. J. Vasile, C. Biddick, and S. Schwalm, J. Vac. Sci. Technol. B **12**, 2388 (1994).

[3]Y. N. Picard, D. P. Adams, and M. J. Vasile, J. Precision Eng. **27**, 59 (2003).

[4]J. P. Sullivan, T. A. Friedmann, and K. Hjort, MRS Bull. **26**, 309 (2001).

[5]E. Kohn, P. Gluche, and M. Adamschik, Diamond Relat. Mater. **8**, 934 (1999).

[6]T. Shibata, Y. Kitamoto, K. Uhno, and E. Makino, J. Microelectromech. Syst. **9**, 47 (2000).

[7]J. Taniguchi, J. Yokoyama, M. Komuro, H. Hiroshima, and I. Miyamoto, Microelectron. Eng. **52**, 415 (2000).

[8]K. F. Jarausch, Ph.D. dissertation: North Carolina State University, (1999).

[9]I. Miyamoto, S. Kiyohara, M. Ide, M. Itami, and S. Honda, Int. J. Jpn. Soc. Prec. Eng. **29**, 295 (1995); A. Olbrich, B. Ebersberger, C. Boit, P. Niedermann, W. Hanni, J. Vancea, and H. Hoffmann, J. Vac. Sci. Technol. A **17**, 1570 (1999).

[10]D. P. Adams, M. J. Vasile, and A. S. M. Krishnan, J. Precision Eng. **24**, 347 (2000).

[11]C. A. Brookers, in *The Properties of Natural and Synthetic Diamond*, edited by J. E. Field (Academic, New York, 1992), p. 515.

[12]J. E. Field, in *Properties and Growth of Diamond*, edited by Gordon Davies (INSPEC, London, 1994), pp. 52–53.

[13]J. Taniguchi, N. Ohno, S. Takeda, I. Miyamoto, and M. Komuro, J. Vac. Sci. Technol. B **16**, 2506 (1998).

[14]P. E. Russell, T. J. Stark, D. P. Griffis, J. R. Phillips, and K. F. Jarausch, J. Vac. Sci. Technol. B **16**, 2494 (1998).

[15]A. Stanishevsky, Thin Solid Films **398-399**, 560 (2001).

[16]Measured previously for graphite substrates, see E. Vietzke, A. Refke, V. Philipps, and M. Hennes, J. Nucl. Mater. **241-243**, 810 (1997).

[17]L. R. Harriott, Jpn. J. Appl. Phys., Part 1 **33**, 7094 (1995).

[18]H. F. Winters and J. W. Coburn, Surf. Sci. Rep. **14**, 161 (1992).

[19]N. N. Efremow, M. W. Geis, D. C. Flanders, G. A. Lincoln, and N. P. Economou, J. Vac. Sci. Technol. B **3**, 416 (1985).

[20]P. E. Russell, D. P. Griffis, G. M. Shedd, T. J. Stark, and J. Vitarelli, U.S. Patent No. 6,140,655 (2000).

[21]T. J. Stark, G. M. Shedd, J. Vitarelli, D. P. Griffis, and P. E. Russell, J. Vac. Sci. Technol. B **13**, 2565 (1995).

[22]A. Datta, Y.-R. Wu, and Y. L. Wang, Appl. Phys. Lett. **75**, 2677 (1999).

[23]P. Sigmund, Phys. Rev. **184**, 383 (1969).

[24]M. J. Vasile, J. Xie, and R. Nassar, J. Vac. Sci. Technol. B **17**, 3085 (1999); M. J. Vasile, R. Nassar, J. Xie, and H. Guo, Micron **30**, 235 (1999).

[25]L. Harriott, Proc. SPIE **773**, 190 (1987).

[26]M. J. Vasile, C. Biddick, and S. Schwalm, Proc. ASME, DSC **46**, 81 (1993).

[27]Atomic force microscopy and interferometric microscopy measurements show an initial surface roughness, R_{rms}, of 2.0–3.0 nm.

[28]This represents the total time to complete a single scan and return to the starting pixel.

[29]*CRC Handbook of Chemistry and Physics*, 79th ed. (CRC, Boca Raton, FL, 1998), pp. 4–140.

[30]TRIM calculations of $Y(\theta)$ model Ga ion impingement on diamond flat surface, assuming a lattice binding energy of 3 eV, a surface binding energy of 7.4 eV, and a displacement energy of 28 eV.

[31]I. Chyr and A. J. Steckl, J. Vac. Sci. Technol. B **19**, 2547 (2001).

[32]R. J. Young, J. R. Cleaver, and H. Ahmed, J. Vac. Sci. Technol. B **11**, 234 (1993).

[33]R. A. Barker, T. M. Mayer, and W. C. Pearson, J. Vac. Sci. Technol. B **1**, 37 (1983); T. Mizutani, C. J. Dale, W. K. Chu, T. M. Mayer, Nucl. Instrum. Methods Phys. Res. B **7/8**, 825 (1985).

[34]J. P. Chang, J. C. Arnold, G. C. H. Zau, H.-Shik Shin, and H. H. Sawin, J. Vac. Sci. Technol. A **15**, 1853 (1997).

[35]T. M. Mayer and R. A. Barker, J. Vac. Sci. Technol. **21**, 757 (1982).

[36]A scan size of 100×100 μm was selected prior to defining the 12×12 μm box. The larger area consists of a 512×512 array of pixels.

[37]E. L. Barish, D. J. Vitkavage, and T. M. Mayer, J. Appl. Phys. **57**, 1336 (1985).

[38]J. Dieleman, F. H. M. Sanders, A. W. Kolfschoten, P. C. Zalm, A. E. de Vries, and A. Haring, J. Vac. Sci. Technol. B **3**, 1384 (1985).

[39]Essentially this condition leads to the formation of a different facet angle under the beam that can have a higher yield; see D. Santamore, K. Edinger, J. Orloff, and J. Melngailis, J. Vac. Sci. Technol. B **15**, 2346 (1997).

[40]A. Datta, Y.-R. Wu, and Y. L. Wang, Phys. Rev. B **63**, 125407 (2001).

[41]T. M. Mayer, E. Chason, and A. J. Howard, J. Appl. Phys. **76**, 1633 (1994).

[42]G. Carter and V. Vishnyakov, Phys. Rev. B **54**, 17647 (1996).

[43]J. Erlebacher, M. J. Aziz, E. Chason, M. B. Sinclair, and J. A. Floro, Phys. Rev. Lett. **82**, 2330 (1999).

[44]R. M. Bradley and J. M. E. Harper, J. Vac. Sci. Technol. A **6**, 2390 (1988).

[45]S. Park, B. Kahng, H. Jeong, and A.-L. Barabasi, Phys. Rev. Lett. **83**, 3486 (1999); M. A. Makeev and A.-L. Barabasi, Appl. Phys. Lett. **71**, 2800 (1997).

[46]C. Herring, *Physics of Powder Metallurgy* (McGraw-Hill, New York, 1951), p. 143.

[47]E. Chason, T. M. Mayer, B. K. Kellerman, D. T. McIlroy, and A. J. Howard, Phys. Rev. Lett. **72**, 3040 (1994).

[48]S. M. Rossnagel, R. S. Robinson, and H. R. Kaufman, Surf. Sci. **123**, 89 (1982).

[49]S. W. MacLaren, J. E. Baker, N. L. Finnegan, and C. M. Loxton, J. Vac. Sci. Technol. A **10**, 468 (1992).

[50]E. A. Eklund, R. Bruinsma, J. Rudnick, and R. S. Williams, Phys. Rev. Lett. **67**, 1759 (1991).

[51]T. M. Mayer, D. P. Adams, and M. J. Vasile (unpublished).

[52]I. Koponen, M. Hautala, and O. P. Sievänen, Phys. Rev. Lett. **78**, 2612 (1997); S. Habenicht, K. P. Lieb, W. Bolse, U. Geyer, F. Roccaforte, and C. Ronning, Nucl. Instrum. Methods Phys. Res. **161−163**, 958 (2000).

[53]G. Carter, J. Appl. Phys. **85**, 455 (1999).

[54]Previous FIB sputtering (without gas assist) by Datta *et al.* (Ref. 40) shows the onset of ripples in diamond at $\theta = 40°$ for $E = 50$ keV and at $\theta = 50°$ for $E = 10$ keV.

[55]D. P. Adams, T. M. Mayer, and M. J. Vasile (unpublished).